Facile and cost-effective methodology to fabricate MoS_2 counter electrode for efficient dye-sensitized solar cells

Dhanasekaran Vikraman[a,g], Supriya A. Patil[b,c], Sajjad Hussain[d,e], Naveed Mengal[f], Hyun-Seok Kim[a], Sung Hoon Jeong[f], Jongwan Jung[d,e], Hak-Sung Kim[b,c,**], Hui Joon Park[g,h,*]

[a] Division of Electronics and Electrical Engineering, Dongguk University-Seoul, Seoul 04620, Republic of Korea
[b] Department of Mechanical Engineering, Hanyang University, Seoul 04763, Republic of Korea
[c] Institute of Nano Science and Technology, Hanyang University, Seoul 04763, Republic of Korea
[d] Graphene Research Institute, Sejong University, Seoul 05006, Republic of Korea
[e] Institute of Nano and Advanced Materials Engineering, Sejong University, Seoul 05006, Republic of Korea
[f] Department of Organic and Nano Engineering, Hanyang University, Seoul 04763, Republic of Korea
[g] Department of Energy Systems Research, Ajou University, Suwon 16499, Republic of Korea
[h] Department of Electrical and Computer Engineering, Ajou University, Suwon 16499, Republic of Korea

ARTICLE INFO

ABSTRACT

Interests in the development of economical and high-efficiency counter electrodes (CEs) of dye-sensitized solar cell (DSSC) to replace the excessively cost and scarce platinum (Pt) CEs have been increased. In this report, we demonstrate a facile chemical bath deposition (CBD) route to prepare layered MoS_2/fluorine-doped tin oxide (FTO) films that directly act as the CEs of DSSCs. A DSSC containing the CBD-synthesized MoS_2/FTO CE (prepared at 0.03 M Mo source concentration, 90 °C bath temperature and 30 min deposition time) exhibits high power conversion efficiency (PCE) of 7.14%, which is approaching that of DSSC with Pt/FTO CE (8.73%). The electrocatalytic activity of the MoS_2/FTO and Pt/FTO CEs are discussed in detail with their cyclic voltammetry (CV), Tafel polarization curves, and electrochemical impedance spectra (EIS). The observed results indicate that our low-cost CE has a high electrocatalytic activity for the reduction of triiodide to iodide and a low charge transfer resistance at the electrolyte–electrode interface with a comparable state to that of a Pt/FTO CE.

1. Introduction

The development of green alternatives to energy generation is essential to preserve the global environment for future generations. Photovoltaics (PVs) offer a clean solution to the energy and environmental crisis. Widespread research has been carried out in the area of dye-sensitized solar cells (DSSCs) since 1991, and this interest is due to their low-cost and simple fabrication process, excellent durability, and relatively high efficiency [1–3]. DSSCs are a promising third-generation PV device, which can be easily and economically fabricated using mesoporous-TiO_2 structure, on which dyes are absorbed, an electrolyte (usually a redox mediator such as iodide/triiodide), and a counter electrode.

The counter electrode (CE) reduces the oxidized electrolyte, which is crucial for high-efficiency DSSCs [4,5], and a noble metal such as platinum (Pt) is conventionally used as a CE material because of its excellent electrical conductivity and high catalytic activity [6].

However, Pt is expensive and scarce, and therefore alloying Pt with various transition metals including Mo, Fe, Co, Pd, Cu and Ni has been studied as a candidate to enhance electrocatalytic activity and to reduce the fabrication cost of the preferred Pt catalysts [7–13]. Remarkably, low content Pt has effectively enhanced the efficiency of the resultant alloys compared with that of the conventional Pt electrode [7,11,14–16]. Moreover, various approaches to replace Pt and its alloys to Pt-free alloy-based electrocatalysts (*e.g.* PdNi, CoNi) have been also suggested [13,17–20].

Meanwhile, cost-effective, chemically stable, and high-performance Pt-free CE materials such as conducting polymers [21], carbonaceous materials [22–24], and inorganic compounds [25,26] have been widely investigated. Especially, transition metal dichalcogenides (TMDs), which is a class of two-dimensional (2D) layered crystals [27,28], attracting much interest as a graphene alternative [29], have shown its potentials as a Pt-free CE material, and TMD-based CEs have shown even better electrochemical stability than that of standard Pt CE in

iodine-based electrolytes under ambient conditions [30,31]. Molybdenum disulfide (MoS$_2$), from the family of TMDs [32–34], is an attractive CE material for DSSCs. MoS$_2$ is made up of three atom layers: two S layers and a Mo layer sandwiched between the two S layers. The three layers are stacked and held together by weak van-der Waals interactions. Advantageously, MoS$_2$ has abundant exposed active sulfur edges, and it has been confirmed, both theoretically and experimentally, that the catalytic activity of MoS$_2$ originates from the active sulfur edges [35,36]. Many researchers have applied commercial MoS$_2$ with different structures and morphologies as the CE material for DSSC applications, proving their potentials [37–40]. A variety of strategies has been explored to prepare MoS$_2$ CEs, such as radio-frequency sputtering, pulsed electrochemical deposition, and hydrothermal processes [32,34,41]. Furthermore, carbon materials (such as graphene sheets and carbon nanotubes) and polymers have been combined with MoS$_2$ to yield composite CEs for DSSCs [42,43]. For example, Li et al. reported a power conversion efficiency (PCE) of 8.01% using a MoS$_2$/graphene CE prepared by an electrochemical method, and the PCE is comparable to that of a Pt CE (8.21%) [44]. However, the reported experimental procedure requires sophisticated instrumental facilities and a clean room environment; consequently, it is not cost-effective, and it is time-consuming.

In this work, we report a facile chemical route to synthesize MoS$_2$ layers directly onto fluorine-doped tin oxide (FTO) by utilizing ammonium heptamolybdate tetrahydrate ((NH$_4$)$_6$Mo$_7$O$_{24}$·4H$_2$O) and thiourea (CH$_4$N$_2$S). The MoS$_2$ atomic layers were systematically investigated to optimize the growth of MoS$_2$ for best use as a CE. On using the MoS$_2$ film as CEs in a DSSC, we found that the devices have excellent electrical conductivity and electrocatalytic activity; furthermore, a PCE of 7.14% was obtained for the MoS$_2$ CE, which is approaching that of a Pt CE (8.73%) under the simulated solar illumination of 100 mW cm^{-2} (AM 1.5).

2. Materials and methods

2.1. Synthesis of MoS$_2$ on FTO substrates

A low-cost and simple chemical bath deposition (CBD) process was used to synthesize the MoS$_2$ atomic layers. Fluorine-doped tin oxide (FTO)-coated substrates with a size of 2 × 2 cm^2 were used for the film preparation process. All the substrates were cleaned using acetone, isopropyl alcohol (IPA), and deionized (DI) water, followed by the drying and baking of the substrates for 5 min. MoS$_2$ atomic layers were grown by CBD using a precursor solution bath containing 0.01–0.03 M ammonium molybdate ((NH$_4$)$_6$Mo$_7$O$_{24}$) and 0.5 M thiourea (CH$_4$N$_2$S; purity 99%, analytical reagent grade, Sigma-Aldrich). The concentration of thiourea was fixed, because MoS$_2$ growth was optimized at that condition. Hydrochloric acid (HCl) was used to control the solution pH (10 ± 0.1) and the reaction rate. The deposition time was varied from 5 to 60 min to grow MoS$_2$ layers of different thicknesses. The bath temperatures used were 80 and 90 °C. The reaction took place in the presence of hydrazine hydrate (N$_2$H$_4$, 1.0 M). The MoS$_2$ layers were post-annealed at 450 °C for 60 min under S environment to improve the crystalline quality of the layers. Then, the samples were rapidly cooled to room temperature. The carrier gas flow rate was kept at 100 sccm during the annealing process, and the pressure of the chamber was maintained at 2 × 10^{-2} Torr.

2.2. Characterization of MoS$_2$ layers

The synthesized MoS$_2$ films were analyzed by Raman spectroscopy (Renishaw inVia RE04, 512-nm Ar laser) using a spot size of 1 μm and a scan speed of 30 s. X-ray diffraction (XRD) measurements were performed on a Rigaku D/max-2500 diffractometer, using Cu-K_α radiation as the X-ray source in the range of 10–90°. Mo and S photoelectron reflection spectra were analyzed using X-ray electron spectroscopy

(XPS) (PHI 5000 Versa Probe, 25 WAl K_α, 6.7 × 10^{-8} Pa). Photoluminescence (PL) spectra were recorded at room temperature with an HORIBA microspectrometer (Jobin Yvon, LabRam HR Evolution) using a Nd:YAG laser (532 nm) with a spot size of 1 μm. Field-emission scanning electron microscopy (FE-SEM, JEOL JSM-6700F) was employed to analyze the morphology and thickness of the films.

2.3. DSSC device fabrication

Dye-sensitized solar cells (DSSCs) were prepared to evaluate the performance of the MoS$_2$ films as counter electrodes (CEs). The detailed fabrication procedures are described elsewhere [37,45]. In brief, a thin TiO$_2$ blocking layer (100 nm) was deposited onto FTO glass substrate by immersing the FTO substrate in 0.1 M TiCl$_4$ for 45 min at 70 °C followed by annealing the substrate at 450 °C for 30 min in air. A 4-μm-thick TiO$_2$ layer with an average particle size of ~20 nm was coated on to FTO substrate by the doctor blade method. The TiO$_2$-coated FTO was then sintered in five steps of 70, 325, 375, 450, and 500 °C for 30, 5, 5, 15, and 15 min, respectively, in a high-temperature furnace (Lab house Co.). A light scattering TiO$_2$ layer (~3 μm) was applied over the previously deposited TiO$_2$ and sintered again at 450 °C for 30 min. Finally, the as-prepared FTO/TiO$_2$ film was sensitized with 0.5 mM N719 (ditetrabutylammonium *cis*-bis(isothiocyanato) bis(2,2′-bipyridyl-4,4′-dicarboxylato)ruthenium(II)) in an absolute ethanol:acetonitrile (1:1) solutions for 24 h. The Pt-coated CE were prepared by spreading a drop of 2 mM chloroplatinic acid hexahydrate (H$_2$PtCl$_6$) in isopropanol onto the FTO substrates and heating to 400 °C for 10 min under ambient air. The dye-sensitized TiO$_2$ with an active area of 0.25 cm^2 and the as-fabricated CE were assembled using a 50-μm-thick spacer polyimide adhesive tape. The polymer electrolyte, which was prepared using 0.1 M LiI, 0.6 M 1-propyl-2,3-dimethylimidazolium iodide, 0.05 M I$_2$, 0.5 M 4-*tert*-buylpyridine, and 3% w/w polyethylene oxide (M_w 250,000) with 5 ml acetonitrile as a solvent, was then injected between the two electrodes.

2.4. Photoelectrochemical measurements

A solar simulator (150-W Xe lamp, Sun 2000 solar simulator, ABET Technologies, USA) equipped with an AM 1.5G filter was used to generate simulated sunlight with a corrected intensity of 100 mW cm^{-2}. The current density-voltage (*J-V*) spectra of DSSCs with different MoS$_2$/FTO and Pt/FTO CEs were obtained using a Keithley 2400 source meter. The cyclic voltammetry (CV) was performed using a three electrode system and iodine-based electrolyte consisting of 10 mM lithium iodide(LiI), 1 mM iodine (I$_2$) and 0.01 M lithium perchlorate (LiClO$_4$) in 200 ml acetonitrile solvent at scan rate of 10 mV s^{-1}. Electrochemical impedance spectroscopy (EIS) spectra were obtained using CompactStat (IviumStat Technologies, Netherlands). The frequency of the applied sinusoidal AC voltage signal was varied from 150 kHz to 0.1 mHz. The polarization measurements were performed at a scan rate of 10 mV s^{-1}. For the EIS and polarization measurements, the symmetrical dummy cells were assembled with two identical CEs filled with the same electrolyte as that used in the DSSCs.

3. Results and discussion

A facile chemical bath deposition (CBD) technique was used to prepare MoS$_2$ with atomic layer thickness on the FTO substrates. Different concentrations of ammonium molybdate were used, from 0.01 to 0.03 M, to optimize the efficient growth of the electrocatalytic MoS$_2$ CE. The deposition bath temperatures used were 80 and 90 °C. The deposition time was changed from 5 to 60 min to investigate the effect of layer thickness on the electrocatalytic ability. The as-prepared atomic layers were subjected to post-deposition annealing at 450 °C in an S environment to improve their crystallinity.
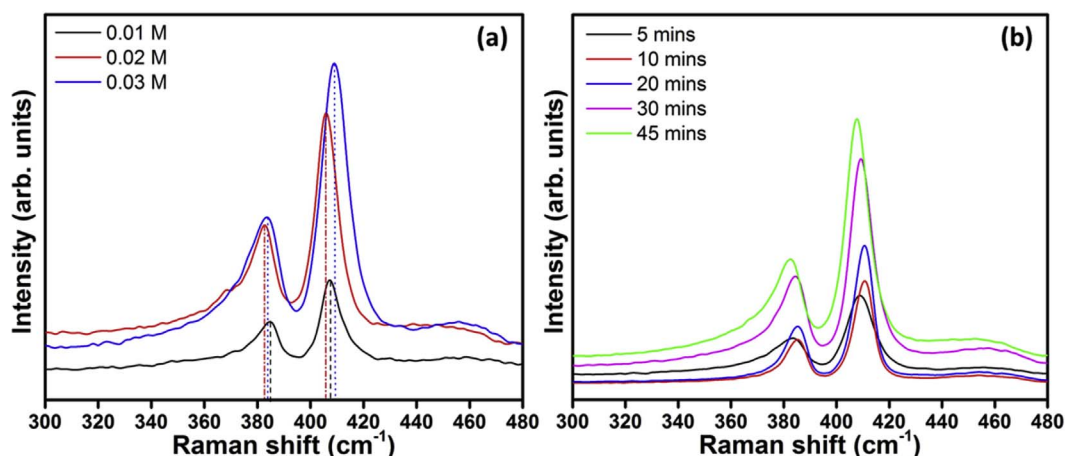
Fig. 1. Raman spectra of MoS_2 layers prepared onto FTO substrates using (a) different concentration of Mo source at 5 min deposition time and 90 °C bath temperature and (b) different deposition time at 0.03 M Mo source and 90 °C bath temperature.

The concentration of ammonium molybdate (Mo source) and the deposition time in CBD play a key role in the growth of MoS_2 layers. The Raman spectra of the MoS_2 layers with 0.01–0.03 M Mo source concentrations (5 min deposition time and 90 °C bath temperature) are shown in Fig. 1a. In the spectrum of the sample prepared with a 0.01 M Mo source, the E_{2g}^1 mode, associated with the in-plane vibrations of S atoms, and A_{1g} mode, associated with the out-of-plane vibrations of the Mo and S atoms, peaks are observed at ~ 384.63 and $\sim 407.28\ cm^{-1}$, respectively. The difference between the E_{2g}^1 and A_{1g} mode peaks (Δk) is $\sim 22.65\ cm^{-1}$, which corresponds to tri-layer MoS_2 [46,47]. In the case of the sample deposited using a 0.02 M Mo source, the E_{2g}^1 and A_{1g} peaks are observed at $\sim 382.74\ cm^{-1}$ and $\sim 405.87\ cm^{-1}$, respectively, with a Δk value of $\sim 23.13\ cm^{-1}$, corresponding to tetra-layer MoS_2 [48]. The Raman spectrum of the MoS_2 atomic layer prepared with 0.03 M precursor concentration contains E_{2g}^1 and A_{1g} peaks at $\sim 383.48\ cm^{-1}$ and $\sim 408.93\ cm^{-1}$, respectively, with Δk, 25.45 cm^{-1}, corresponding to few-layered MoS_2 [46,49]. The Raman spectra of MoS_2 atomic layers with 5, 10, 20, 30, and 45 min deposition time (0.03 M precursor concentration and 90 °C bath temperature) are shown in Fig. 1b. The two characteristic phonon modes of Raman spectra are shown in the range of 382–385 cm^{-1} (E_{2g}^1 mode) and 407–410 cm^{-1} (A_{1g} mode). As the deposition time increased, the intensities of peaks as well as the layer thickness increased (Fig. 1b). The formation of the MoS_2 layer with a bath temperature 80 °C was also investigated at different precursor concentrations and deposition times, and the Raman spectra of the corresponding samples are given in Fig. S1.

X-ray electron spectroscopy (XPS) analysis was performed to measure the Mo and S binding energies. For the MoS_2 prepared by 0.01 M Mo source (5 min deposition time and 90 °C bath temperature), Mo^{4+} 3d peaks are observed at 227.9 and 231.2 eV (Fig. 2a), which are attributed to the doublet of $Mo^{4+}\ 3d_{5/2}$ and $Mo^{4+}\ 3d_{3/2}$, respectively [50], and a weak S 2s peak is observed at 225.3 eV (Fig. 2a). Furthermore, S 2p-related peaks are observed at 161.1 and 162.4 eV, arising from S $2p_{3/2}$ and S $2p_{1/2}$, respectively (Fig. 2b). The binding energies varied slightly with precursor concentrations, such as 0.02 and 0.03 M, which could be attributed to the increment in the number of layers. The results are in good agreement with the reported values for MoS_2 crystals [51].

The surface morphologies of the MoS_2 layers were investigated in more detail using scanning electron microscopy (SEM), and the images of MoS_2 layers prepared using different Mo source concentration (90 °C bath temperature and 5 min deposition time) are shown in Fig. 3a–c. As for the MoS_2 layers prepared with 0.01 M concentration Mo precursor, a smooth surface consisting of spherical shaped grains without any agglomeration was found (Fig. 3a), and uniformly distributed grains

became more discernible on the surface of the layers as the Mo concentration increased to 0.03 M (Fig. 3b and c). These layers are compact and dense, and the surfaces are free from pin-holes, cracks, and voids. From these images, we confirm that the growth of MoS_2 follows homogeneous nucleation as the thickness of the layer increases. The morphological evolution provides valuable insights into the surface formation processes during the layer growth. Meanwhile, further increased deposition time (30 and 45 min at 0.03 M Mo source and 90 °C bath temperature) generates larger agglomerations of uniform spherical grains with voids as shown in Fig. 3d and e. Additionally, the AFM thickness profile spectra are provided in Fig. S2 with their 2D images (inset of Fig. S2), and it was confirmed that the film thickness increased with the deposition time.

The X-ray diffraction (XRD) patterns of MoS_2 layers prepared with different Mo source concentration (5 min deposition time and 90 °C bath temperature) are shown in Fig. 4a. The (002) lattice-oriented peak, corresponding to the preferential orientation, is observed at $2\theta = 13.85°$, which is in good agreement with previous results [52,53]. The XRD results provide convincing evidence confirming the MoS_2 layer structure. The luminescence properties of the MoS_2 atomic layers were investigated by photoluminescence (PL) spectroscopy (Fig. 4b). The PL spectra of MoS_2 prepared with different Mo precursor concentration (5 min deposition time and 90 °C bath temperature) are shown in Fig. 4b. The PL spectrum of the MoS_2 layer prepared using 0.01 M Mo source contains a broad and intense luminescence peak at 705 nm (1.75 eV) and a smaller peak at 741 nm (1.66 eV) (Fig. 4b). The main emission peak corresponds to the band gap of the materials, and the latter peak could be attributed to the valence band splitting caused by strong spin-orbit coupling, which corresponds to the direct excitonic transition at the K-point of the Brillouin zone of MoS_2 [54–56]. The measured energy difference (~ 0.09 eV) is in close agreement with that in the literature [54,57]. Additionally, two sharp PL peaks at ~ 572 and 580 nm were observed, and these are associated with the surface recombination of quantum-confined MoS_2 [58,59] and the surface states of the MoS_2 [60,61]. Meanwhile, the luminescence peak intensity decreased with increasing precursor concentrations, which might be due to the increase in the film thickness (Fig. 4b). The optical absorption of the MoS_2 atomic layer was investigated using UV-visible spectroscopy. The absorption peaks, observed at 392, 451, 620, and 676 nm (Fig. 4c), correspond to the characteristic absorption bands of earlier reported MoS_2 samples [62–65]. Excitonic peaks at 676 (A) and 620 nm (B), arising from the K-point of the Brillouin zone, can be clearly seen, and the threshold observed at ~ 392 (D) and ~ 451 nm (C) can be assigned to the direct transition from the deep valence band to the conduction band [59,66]. The absorption peaks observed in the near-UV region ($\lambda < 300$ nm) can be attributed to the excitonic features of the MoS_2
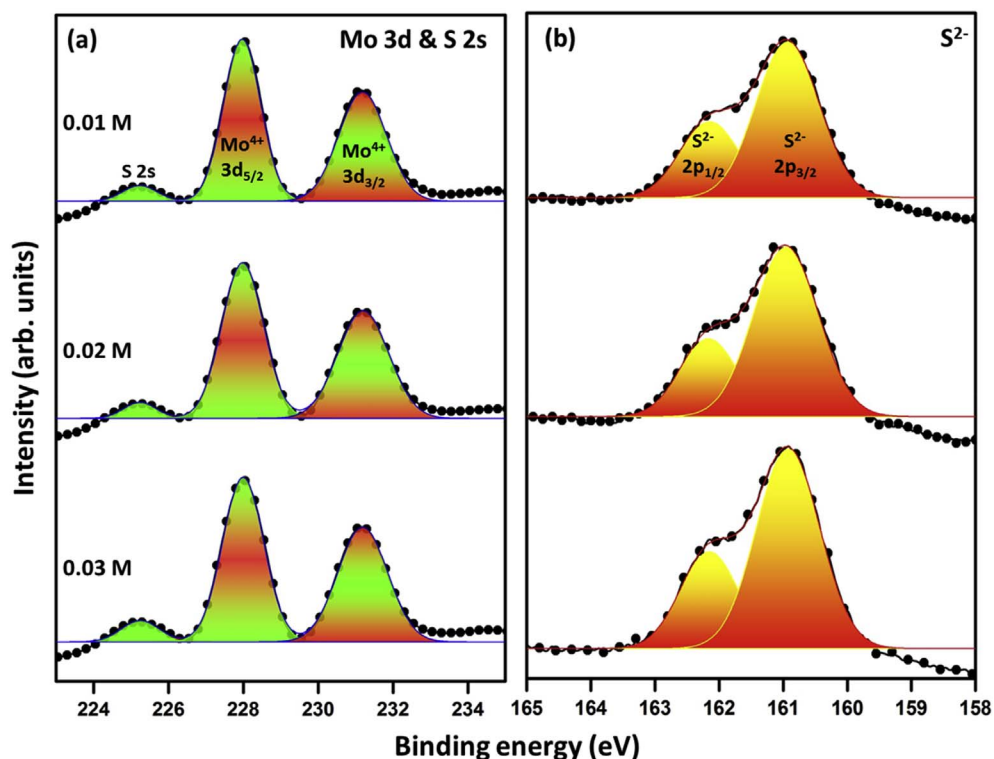
Fig. 2. XPS spectra of MoS_2 layers prepared using different Mo source concentrations at 5 min deposition time and 90 °C bath temperature: (a) Mo and S and (b) S atoms binding energy spectra.

[56]. The peaks are slightly red-shifted with an increase in the layer thickness. The film transparency is diminished with increasing layer thickness [55,67].

The current density–voltage (J–V) curves of DSSCs with MoS_2/FTO and Pt/FTO CEs were obtained under simulated solar illumination (AM 1.5G) with a light intensity of 100 mW cm^{-2}. A schematic representation of the DSSCs using MoS_2/FTO CE is given in Fig. 5a. As summarized in Table S1, the performances of MoS_2/FTO CE-based DSSC were maximized at 30 min CBD deposition time condition (0.03 M Mo source and 90 °C bath temperature); that is, an efficiency of 7.14% (short circuit current density (J_{sc}) = 15.92 mA cm^{-2}, open-circuit voltage

(V_{oc}) = 0.73 V, and fill factor (FF) = 0.61), and these values are approaching those of a Pt/FTO CE with an efficiency of 8.73% (J_{sc} = 17.84 mA cm^{-2}, V_{oc} = 0.71 V, and FF = 0.69). The J-V characteristic curves of DSSCs with MoS_2/FTO and Pt/FTO CEs and their performances under the same illumination conditions are represented in Fig. 5b and Table 1.

The performances of DSSCs with MoS_2-based CE were improved as the deposition time increased, because the larger agglomerations of uniform spherical grains, grown for longer deposition time (Fig. 3), have a large surface area with numerous edge sites, which promote the electrocatalytic activity. However, their performances were degraded
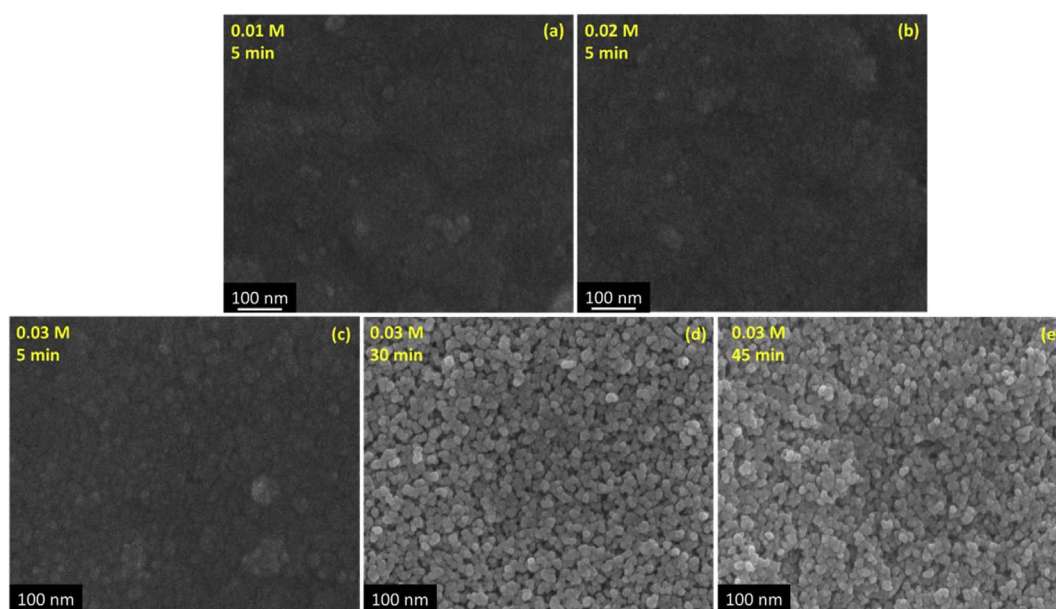

Fig. 3. SEM images of MoS_2 layers: (a–c) according to different Mo source concentrations (0.01–0.03 M) at 5 min deposition time and 90 °C bath temperature. (c–e) according to different deposition time (5–45 min) at 0.03 M Mo source concentration and 90 °C bath temperature.
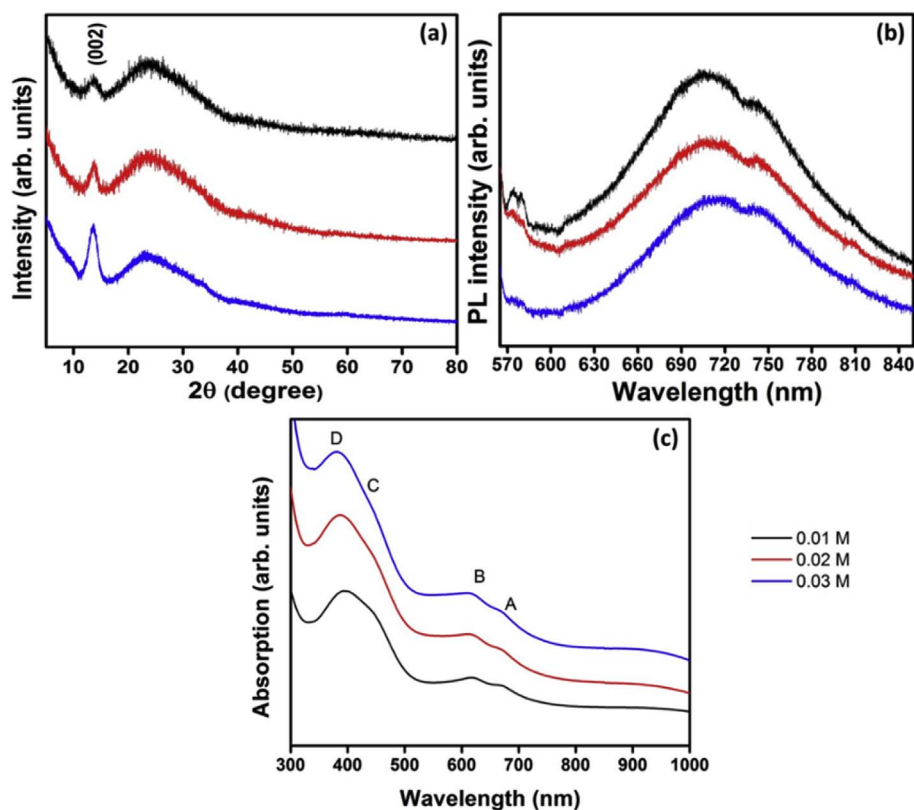
Fig. 4. (a) XRD patterns, (b) PL spectra and (c) UV-visible spectroscopy spectra of MoS_2 layers prepared with different Mo source concentrations at 5 min deposition time and 90 °C bath temperature.

with MoS_2, grown for 45 min deposition time. To understand the performance degradation of MoS_2/FTO CE-based DSSCs prepared by longer deposition time condition (@ 45 min), the structural properties of the CBD-deposited MoS_2 atomic layers, at different deposition time (10–45 min) conditions (with 0.03 M Mo source concentration and 90 °C bath temperature), were further investigated by XRD patterns. The preferential orientation of (002) peak intensity is slightly varied with increase of deposition time as shown in Fig. S3. In addition to preferential lattice plane, some novel peaks are emerged with increase of deposition time. Due to increase of deposition time as well as layer thickness of MoS_2, different to the XRD pattern of 5 min deposition sample that have the preferentially oriented (002) peak (Fig. 4a), (004), (102), (103), (006), (105), and (112) lattice planes of MoS_2 were additionally observed (JCPDS–87–2416) from those of 30 min deposition sample (Fig. S3). Moreover, as the deposition time was further increased to 45 min, (004) lattice orientation was exhibited as a preferential orientation and (104) and (106) lattice planes also became discernible (Fig. S3), suggesting that layered MoS_2 structure turned

Table 1
Solar cell and EIS parameters of DSSCs with MoS_2/FTO and Pt/FTO counter electrodes.

Type of CEs	V_{OC} (V)	J_{SC} (mA·cm^{-2})	FF	PCE (%)	R_S (Ω·cm^2)	R_{CT} (Ω·cm^2)	E_{PP} (mV)
MoS_2 (30 min)	0.73	15.92	0.61	7.14	8.34	25.77	352
Pt	0.71	17.84	0.69	8.73	7.21	16.69	357

toward bulk. In addition, (002) lattice oriented Mo_2S_3 (JCPDS–89–5113) phase peak (indicated with * in Fig. S3) was observed in 45 min deposition sample. Consequently, the longer deposition time (@ 45 min) initiates the change of the layered structure to bulk and the phase transformation from MoS_2 to Mo_2S_3, as indicated in the XRD patterns. This would directly decrease the number of active sulfur site of MoS_2 structure, which could affect its catalytic properties significantly and degrade the performances of solar cells. Similarly, it has been reported that the edge sites of the 2D material are highly
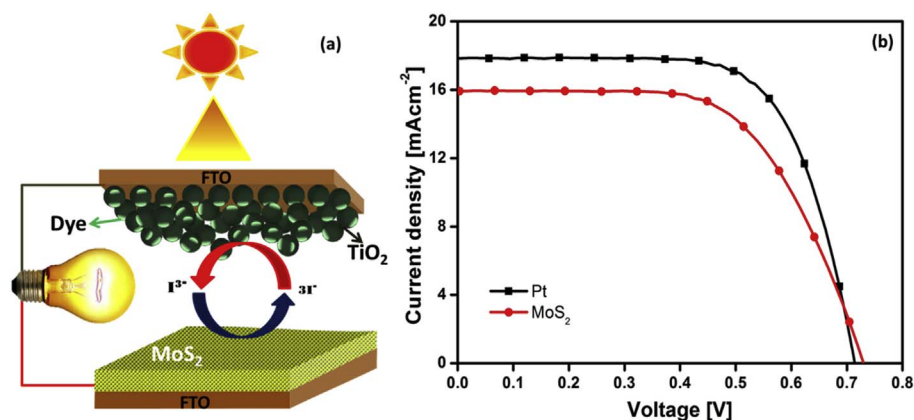

Fig. 5. (a) Schematic diagram of DSSCs using MoS_2/FTO as a CE; (b) J-V characteristics of DSSCs with MoS_2/FTO and Pt/FTO counter electrodes.

active compared to the basal sites [68]. Meanwhile, the structural change of MoS_2 at longer deposition time conditions was further confirmed by the PL spectra (Fig. S4), and it was shown that the QD surface state related peaks (~ 580 nm) eventually disappeared in the MoS_2 prepared at longer deposition times, unfavorable to their electrocatalytic properties.

From the reflection peak width of XRD data, the crystal size of MoS_2 layers (*D*) was determined by the Debye-Scherrer's relation using equation (1); [69]

$$D = \frac{K\lambda}{\beta \cos \theta} \qquad (1)$$

where λ is the X-ray wavelength and *K* is the particle shape factor, taken as 1 in all cases. β is defined as the line-broadening at half-maximum of the peak (FWHM) after subtracting the instrumental line broadening, and θ is the position (angle) of the peak. The estimated values of crystallite size are 2.93, 2.94, 2.96, 2.97 and 3.17 nm for MoS_2 prepared using 5, 10, 15, 20 and 30 min, respectively. For these estimations, the (002) preferential peak has been used. For 45 min deposited MoS_2, the crystallite size is enormously increased to 15.8 nm which is predicted using (004) lattice preferential peak.

To investigate the electrocatalytic performance of our MoS_2/FTO CE, we carried out cyclic voltammogram (CV) using three electrode system. For the evaluation of reaction kinetics and the electrocatalytic activities of the MoS_2/FTO and Pt/FTO CEs toward the reduction of I_3^-, the CV measurements were conducted in a 3-methoxypropionitrile solution consisting of 50 mM LiI, 10 mM I_2, and 500 mM $LiClO_4$ at a scan rate of 10 mV s^{-1}. From the CVs curves of MoS_2/FTO and Pt/FTO and CEs (Fig. 6a), two redox pairs were observed (Ox-1/Red-1, Ox-2/Red-2), where the first pair is associated with the redox reaction of I_3^-/I^-, and the later pair is related to the redox reaction of I_2/I_3^- [70]. The Ox-1/Red-1 peaks correspond to the reaction shown in equation (2), while the Ox-2/Red-2 peaks correspond to that shown in equation (3).

$$I_3^- + 2e^- \leftrightarrow 3I^- \qquad (2)$$

$$3I_2 + 2e^- \leftrightarrow 2I_3^- \qquad (3)$$

Because the CE of a DSSC is responsible for catalyzing the reduction of I_3^- to I^-, the characteristic Ox-1 and Red-1 peaks are the focus of our analysis. The value of anodic peak to cathodic peak separation (E_{pp}), an important parameter for comparing catalytic activities of different CEs [71], was found to be less for the MoS_2/FTO CE (352 mV) than that of Pt/FTO (357 mV), indicating a comparable electrocatalytic activity of MoS_2/FTO CE for the reduction of I_3^- to that of Pt/FTO CE (Fig. 6a and Table 1), and this is due to the large specific surface area and more active edge sites of MoS_2. The MoS_2/FTO and Pt/FTO CEs have cathodic peak potentials 0.355 and 0.365 V, respectively. Additional CVs were measured for the I_3^-/I^- redox reaction of the MoS_2 CEs at different scan rates (10–100 mV s^{-1}) (Fig. 6b), and it was confirmed that the current peak values increased linearly with the scan rate, representing that the inner sites of MoS_2 also became reactive and were catalytically active [38,72]. To demonstrate the electrochemical stability of MoS_2 CE, CV was recorded for 50 consecutive cycles with a potential ranging from -0.2–1 V. As shown in Fig. S5, even after 50 consecutive scans, the CV curve shapes of MoS_2 CE were not noticeably changed, and their redox peak current values (cathodic and anodic peak current density) were almost constant, which suggested that the MoS_2 CE had reversible redox activity, excellent electrochemical and chemical stability, and strong adhesion to the FTO glass substrate [26,73–75]. The superior electrochemical stability of MoS_2 CE is expected to provide long-term stability of solar cell devices [75].

To further elucidate the catalytic activities of different CEs on the reduction of triiodide, electrochemical impedance spectroscopy (EIS) experiments were carried out using symmetric cells fabricated with two identical electrodes (CE/electrolyte/CE). The Nyquist plots (Fig. 6c) of the symmetric cells with different CEs illustrate the impedance characteristics, represented by semicircles, and the parameters are
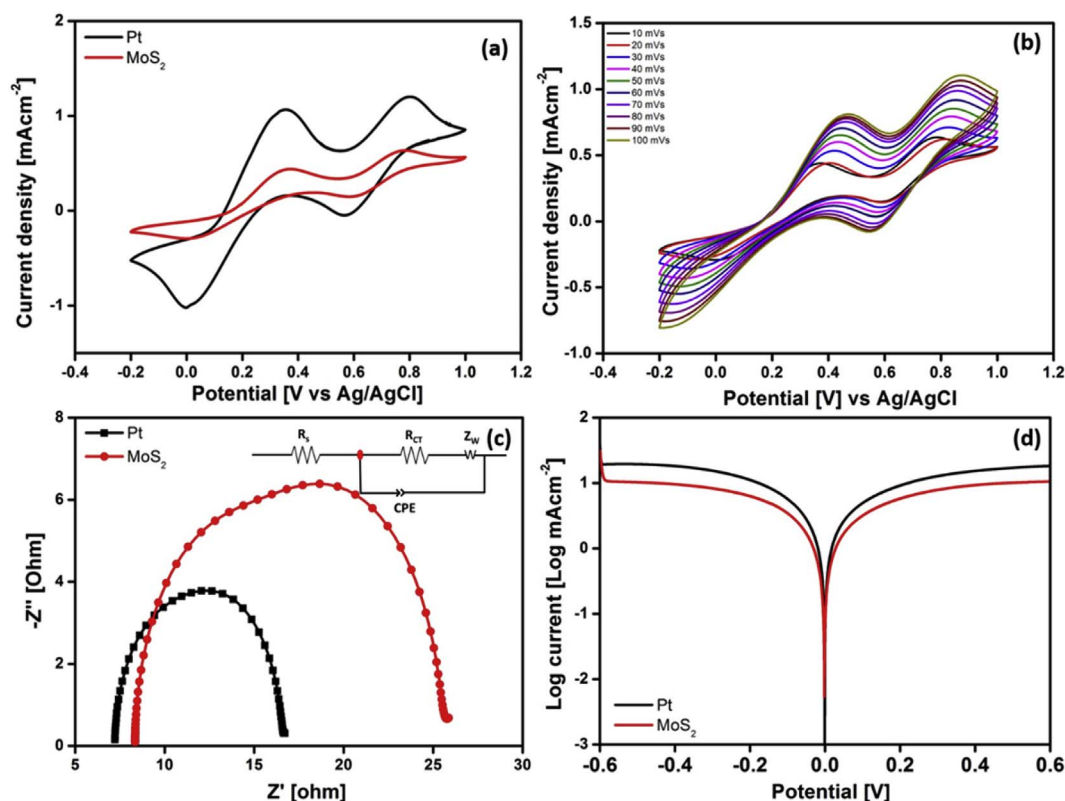

Fig. 6. (a) CVs of I_3^-/I^- redox system using MoS_2/FTO and Pt/FTO CEs (scan rate of 10 mV s^{-1}). (b) CVs of I_3^-/I^- redox system using MoS_2/FTO CEs at various scan rate (10–100 mV s^{-1}). (c) Nyquist plots of MoS_2/FTO and Pt/FTO CEs with inset as an equivalent circuit. (d) Tafel polarization curves of symmetrical cells with MoS_2/FTO and Pt/FTO CEs.

summarized in Table 1. According to the Randles-type circuit (inset of Fig. 6c), the frequency intercept on the real axis represents the series resistance (R_S). The estimated R_S value of the MoS_2/FTO is at $8.34\,\Omega\,cm^2$, which is a closer value to that of a Pt/FTO electrode ($7.21\,\Omega\,cm^2$). The semicircle indicates the charge-transfer resistance (R_{CT}) and the corresponding capacitance (CPE) in the charge-transfer process for reduction of triiodide at the electrolyte/CE interface. The Nernst diffusion impedance (Z_W) represents the I^-/I_3^- redox couple transport in the electrolyte. The estimated R_{CT} values of the MoS_2/FTO and Pt/FTO CEs are 25.77 and $16.69\,\Omega\,cm^2$, respectively.

Fig. 6d shows the Tafel polarization curves of the symmetric cells prepared by MoS_2/FTO and Pt/FTO CEs. The tangent slope of the anodic or cathodic branches of Tafel curve provides information about the exchange current density, which is closely associated with the electrolyte/CE interface resistance value. A larger slope in the anodic or cathodic branch gives a higher exchange current density on the electrode, representing higher electrocatalytic activity and lower charge-transfer resistance at the electrolyte/CE interface. Fig. 6d demonstrates that the catalytic activity of MoS_2/FTO CE is comparable to that of Pt/FTO CE. From the aforementioned results, we could confirm that the controlled growth of MoS_2 on FTO would be beneficial to develop a low-cost and efficient electrocatalytic CE for DSSCs.

4. Conclusions

According to CV, EIS, and the Tafel analyses, the layered structure of MoS_2, prepared by the facile solution-based CBD method, had outstanding electrocatalytic activities. The MoS_2 layers have a high specific surface area and numerous edge active sites, which increase the electrocatalytic behavior. Finally, a DSSC assembled with the MoS_2/FTO CE exhibited an excellent PCE of 7.14%, approaching that of a DSSC with a conventional Pt/FTO CE (8.73%). This work demonstrates that the layered MoS_2 on FTO grown by CBD could be a low-cost alternative to expensive Pt-containing DSSCs.

Acknowledgement

Appendix A. Supplementary data

Supplementary data related to this article can be found at http://dx.doi.org/10.1016/j.dyepig.2017.12.037.

References

[1] O'regan B, Grfitzeli M. A low-cost, high-efficiency solar cell based on dye-sensitized. Nature 1991;353(6346):737–40.

[2] Mathew S, Yella A, Gao P, Humphry-Baker R, Curchod BF, Ashari-Astani N, et al. Dye-sensitized solar cells with 13% efficiency achieved through the molecular engineering of porphyrin sensitizers. Nat Chem 2014;6(3):242–7.

[3] Kavan L, Yum JH, Grä¨tzel M. Optically transparent cathode for dye-sensitized solar cells based on graphene nanoplatelets. ACS Nano 2010;5(1):165–72.

[4] Boschloo G, Hagfeldt A. Characteristics of the iodide/triiodide redox mediator in dye-sensitized solar cells. Accounts Chem Res 2009;42(11):1819–26.

[5] Hong SY, Kim Y, Park Y, Choi A, Choi N-S, Lee KT. Charge carriers in rechargeable batteries: Na ions vs. Li ions. Energy Environ Sci 2013;6(7):2067–81.

[6] Grätzel M. Photoelectrochemical cells. Nature 2001;414(6861):338–44.

[7] Yang P, Tang Q. Robust counter electrodes from nanoporous NiM (M = Pt, Pd) alloys for dye-sensitized solar cells. Electrochim Acta 2015;182:827–33.

[8] Tang Q, Zhang H, Meng Y, He B, Yu L. Dissolution engineering of platinum alloy counter electrodes in dye-sensitized solar cells. Angew Chem Int Ed Engl. 2015;54(39):11448–52.

[9] Li H, Tang Q, Meng Y, He B, Yu L. Dissolution-resistant platinum alloy counter electrodes for stable dye-sensitized solar cells. Electrochim Acta 2016;190:409–18.

[10] Li Y, Tang Q, Yu L, Yan X, Dong L. Cost-effective platinum alloy counter electrodes for liquid-junction dye-sensitized solar cells. J Power Sources 2016;305:217–24.

[11] Dao V-D, Choi H-S. Pt nanourchins as efficient and robust counter electrode materials for dye-sensitized solar cells. ACS Appl Mater Interfaces 2016;8(1):1004–10.

[12] Zhang H, Tang Q, He B. Alloying of platinum and molybdenum for transparent counter electrodes. A strategy of enhancing power output for bifacial dye-sensitized solar cells. RSC Adv 2015;5(64):51600–7.

[13] Wu J, Lan Z, Lin J, Huang M, Huang Y, Fan L, et al. Counter electrodes in dye-sensitized solar cells. Chem Soc Rev 2017;46(19):5975–6023.

[14] He B, Meng X, Tang Q. Low-cost counter electrodes from CoPt alloys for efficient dye-sensitized solar cells. ACS Appl Mater Interfaces 2014;6(7):4812–8.

[15] Yang Q, Yang P, Duan J, Wang X, Wang L, Wang Z, et al. Ternary platinum alloy counter electrodes for high-efficiency dye-sensitized solar cells. Electrochim Acta 2016;190:85–91.

[16] Wan J, Fang G, Yin H, Liu X, Liu D, Zhao M, et al. Pt–Ni alloy nanoparticles as superior counter electrodes for dye-sensitized solar cells: experimental and theoretical understanding. Adv Mater 2014;26(48):8101–6.

[17] Chen X, Tang Q, He B, Lin L, Yu L. Platinum-free binary Co-Ni alloy counter electrodes for efficient dye-sensitized solar cells. Angew Chem Int Ed Engl. 2014;53(40):10799–803.

[18] Özel F, Sarılmaz A, İstanbullu B, Aljabour A, Kuş M, Sönmezoğlu S. Penternary chalcogenides nanocrystals as catalytic materials for efficient counter electrodes in dye-synthesized solar cells. Sci Rep 2016;6:29207.

[19] Jiang X, Li H, Li S, Huang S, Zhu C, Hou L. Metal-organic framework-derived Ni–Co alloy@carbon microspheres as high-performance counter electrode catalysts for dye-sensitized solar cells. Chem Eng J 2018;334:419–31.

[20] Gao Z, Wang L, Chang J, Chen C, Wu D, Xu F, et al. CoNi alloy incorporated, N doped porous carbon as efficient counter electrode for dye-sensitized solar cell. J Power Sources 2017;348:158–67.

[21] Ke C-R, Chang C-C, Ting J-M. Modified conducting polymer films having high catalytic activity for use as counter electrodes in rigid and flexible dye-sensitized solar cells. J Power Sources 2015;284:489–96.

[22] Wang H, Hu YH. Graphene as a counter electrode material for dye-sensitized solar cells. Energy Environ Sci 2012;5(8):8182–8.

[23] Wang H, Sun K, Tao F, Stacchiola DJ, Hu YH. 3D honeycomb-like structured graphene and its high efficiency as a counter-electrode catalyst for dye-sensitized solar cells. Angew Chem 2013;125(35):9380–4.

[24] Wei W, Sun K, Hu YH. Synthesis of 3D cauliflower-fungus-like graphene from CO_2 as a highly efficient counter electrode material for dye-sensitized solar cells. J Mater Chem A 2014;2(40):16842–6.

[25] Gr Li, Wang F, Jiang Qw, Gao Xp, Shen Pw. Carbon nanotubes with titanium nitride as a low-cost counter-electrode material for dye-sensitized solar cells. Angew Chem Int Ed Engl. 2010;49(21):3653–6.

[26] Jang JS, Ham DJ, Ramasamy E, Lee J, Lee JS. Platinum-free tungsten carbides as an efficient counter electrode for dye sensitized solar cells. Chem Commun 2010;46(45):8600–2.

[27] Xu M, Liang T, Shi M, Chen H. Graphene-like two-dimensional materials. Chem Rev 2013;113(5):3766–98.

[28] Butler SZ, Hollen SM, Cao L, Cui Y, Gupta JA, Gutiérrez HR, et al. Progress, challenges, and opportunities in two-dimensional materials beyond graphene. ACS Nano 2013;7(4):2898–926.

[29] Novoselov KS, Fal V, Colombo L, Gellert P, Schwab M, Kim K. A roadmap for graphene. Nature 2012;490(7419):192–200.

[30] Hussain S, Patil SA, Vikraman D, Liu H, Kim H-S, Jung J. High performance $MoSe_2$/Mo counter electrodes based-dye-sensitized solar cells. J Electrochem Soc 2017;164(2):E11–6.

[31] Singh E, Kim KS, Yeom GY, Nalwa HS. Two-dimensional transition metal dichalcogenides-based counter electrodes for dye-sensitized solar cells. RSC Adv 2017;7:28234–90.

[32] Wei W, Sun K, Hu YH. An efficient counter electrode material for dye-sensitized solar cells—flower-structured 1T metallic phase MoS_2. J Mater Chem A 2016;4(32):12398–401.

[33] Bi E, Chen H, Yang X, Peng W, Grätzel M, Han L. A quasi core–shell nitrogen-doped graphene/cobalt sulfide conductive catalyst for highly efficient dye-sensitized solar cells. Energy Environ Sci 2014;7(8):2637–41.

[34] Hussain S, Shaikh SF, Vikraman D, Mane RS, Joo O-S, Naushad M, et al. High-performance platinum-free dye-sensitized solar cells with molybdenum disulfide films as counter electrodes. ChemPhysChem 2015;16(18):3959–65.

[35] Jaramillo TF, Jørgensen KP, Bonde J, Nielsen JH, Horch S, Chorkendorff I. Identification of active edge sites for electrochemical H_2 evolution from MoS_2 nanocatalysts. Science 2007;317(5834):100–2.

[36] Tenne R, Margulis L, Genut Mea, Hodes G. Polyhedral and cylindrical structures of tungsten disulphide. Nature 1992;360(6403):444–6.

[37] Patil SA, Kalode PY, Mane RS, Shinde DV, Doyoung A, Keumnam C, et al. Highly efficient and stable DSSCs of wet-chemically synthesized MoS_2 counter electrode. Dalton Trans 2014;43(14):5256–9.

[38] Yue G, Lin J-Y, Tai S-Y, Xiao Y, Wu J. A catalytic composite film of MoS_2/graphene flake as a counter electrode for Pt-free dye-sensitized solar cells. Electrochim Acta 2012;85:162–8.

[39] Tai S-Y, Liu C-J, Chou S-W, Chien FS-S, Lin J-Y, Lin T-W. Few-layer MoS_2 nanosheets coated onto multi-walled carbon nanotubes as a low-cost and highly electrocatalytic counter electrode for dye-sensitized solar cells. J Mater Chem

2012;22(47):24753–9.

[40] Yue G, Wu J, Xiao Y, Huang M, Lin J, Lin J-Y. High performance platinum-free counter electrode of molybdenum sulfide-carbon used in dye-sensitized solar cells. J Mater Chem A 2013;1(4):1495–501.

[41] Hu Z, Xia K, Zhang J, Hu Z, Zhu Y. Highly transparent ultrathin metal sulfide films as efficient counter electrodes for bifacial dye-sensitized solar cells. Electrochim Acta 2015;170:39–47.

[42] Xin X, He M, Han W, Jung J, Lin Z. Low-cost copper zinc tin sulfide counter electrodes for high-efficiency dye-sensitized solar cells. Angew Chem Int Ed Engl. 2011;50(49):11739–42.

[43] Yue G, Wu J, Xiao Y, Huang M, Lin J, Lin J-Y. High performance platinum-free counter electrode of molybdenum sulfide–carbon used in dye-sensitized solar cells. J Mater Chem A 2013;1(4):1495–501.

[44] Liu C-J, Tai S-Y, Chou S-W, Yu Y-C, Chang K-D, Wang S, et al. Facile synthesis of MoS$_2$/graphene nanocomposite with high catalytic activity toward triiodide reduction in dye-sensitized solar cells. J Mater Chem 2012;22(39):21057–64.

[45] Huang K-C, Wang Y-C, Dong R-X, Tsai W-C, Tsai K-W, Wang C-C, et al. A high performance dye-sensitized solar cell with a novel nanocomposite film of PtNP/MWCNT on the counter electrode. J Mater Chem 2010;20(20):4067–73.

[46] Lee YH, Zhang XQ, Zhang W, Chang MT, Lin CT, Chang KD, et al. Synthesis of large-area MoS$_2$ atomic layers with chemical vapor deposition. Adv Mater 2012;24(17):2320–5.

[47] Li H, Zhang Q, Yap CCR, Tay BK, Edwin THT, Olivier A, et al. From bulk to monolayer MoS$_2$: evolution of Raman scattering. Adv Funct Mater 2012;22(7):1385–90.

[48] Yang J, Gu Y, Lee E, Lee H, Park SH, Cho M-H, et al. Wafer-scale synthesis of thickness-controllable MoS$_2$ films via solution-processing using a dimethylformamide/n-butylamine/2-aminoethanol solvent system. Nanoscale 2015;7(20):9311–9.

[49] Lee C, Yan H, Brus LE, Heinz TF, Hone J, Ryu S. Anomalous lattice vibrations of single-and few-layer MoS$_2$. ACS Nano 2010;4(5):2695–700.

[50] Song I, Park C, Hong M, Baik J, Shin HJ, Choi HC. Patternable large-scale molybdenium disulfide atomic layers grown by gold-assisted chemical vapor deposition. Angew Chem Int Ed Engl. 2014;53(5):1266–9.

[51] Altavilla C, Sarno M, Ciambelli P. A novel wet chemistry approach for the synthesis of hybrid 2D free-floating single or multilayer nanosheets of MS$_2$@oleylamine (M = Mo, W). ýChem Mater 2011;23(17):3879–85.

[52] Zhu YQ, Sekine T, Li YH, Fay MW, Zhao YM, Patrick Poa C, et al. Shock-absorbing and failure mechanisms of WS$_2$ and MoS$_2$ nanoparticles with fullerene-like structures under shock wave pressure. J Am Chem Soc 2005;127(46):16263–72.

[53] Hussain S, Shehzad MA, Vikraman D, Khan MF, Singh J, Choi D-C, et al. Synthesis and characterization of large-area and continuous MoS$_2$ atomic layers by RF magnetron sputtering. Nanoscale 2016;8(7):4340–7.

[54] Splendiani A, Sun L, Zhang Y, Li T, Kim J, Chim C-Y, et al. Emerging photoluminescence in monolayer MoS$_2$. Nano Lett 2010;10(4):1271–5.

[55] Hussain S, Shehzad MA, Vikraman D, Iqbal MZ, Singh J, Khan MF, et al. Controlled synthesis and optical properties of polycrystalline molybdenum disulfide atomic layers grown by chemical vapor deposition. J Alloy Comp 2015;653:369–78.

[56] Chikan V, Kelley D. Size-dependent spectroscopy of MoS$_2$ nanoclusters. J Phys Chem B 2002;106(15):3794–804.

[57] Frey G, Elani S, Homyonfer M, Feldman Y, Tenne R. Optical-absorption spectra of inorganic fullerenelike MS$_2$ (M = Mo, W). Phys Rev B 1998;57(11):6666.

[58] Wilcoxon J, Newcomer P, Samara G. Synthesis and optical properties of MoS$_2$ nanoclusters. Proc Mater Res Soc Symp Proc. Cambridge Univ Press; 1996. p. 371.

[59] Gopalakrishnan D, Damien D, Shaijumon MM. MoS$_2$ quantum dot-interspersed exfoliated MoS$_2$ nanosheets. ACS Nano 2014;8(5):5297–303.

[60] Gopalakrishnan D, Damien D, Li B, Gullappalli H, Pillai VK, Ajayan PM, et al. Electrochemical synthesis of luminescent MoS$_2$ quantum dots. ýChem Commun 2015;51(29):6293–6.

[61] Li H, He X, Kang Z, Huang H, Liu Y, Liu J, et al. Water-soluble fluorescent carbon quantum dots and photocatalyst design. Angew Chem Int Ed Engl. 2010;49(26):4430–4.

[62] Wang H, Lu Z, Xu S, Kong D, Cha JJ, Zheng G, et al. Electrochemical tuning of vertically aligned MoS$_2$ nanofilms and its application in improving hydrogen evolution reaction. Proc Natl Acad Sci 2013;110(49):19701–6.

[63] Wilcoxon J, Newcomer P, Samara G. Synthesis and optical properties of MoS$_2$ and isomorphous nanoclusters in the quantum confinement regime. J Appl Phys 1997;81(12):7934–44.

[64] Wilson J, Yoffe A. The transition metal dichalcogenides discussion and interpretation of the observed optical, electrical and structural properties. Adv Phys 1969;18(73):193–335.

[65] Vikraman D, Akbar K, Hussain S, Yoo G, Jang J-Y, Chun S-H, et al. Direct synthesis of thickness-tunable MoS$_2$ quantum dot thin layers: optical, structural and electrical properties and their application to hydrogen evolution. Nano Energy 2017;35:101–14.

[66] Wilcoxon J, Samara G. Strong quantum-size effects in a layered semiconductor: MoS2 nanoclusters. Phys Rev B 1995;51(11):7299.

[67] Lee Y, Lee J, Bark H, Oh I-K, Ryu GH, Lee Z, et al. Synthesis of wafer-scale uniform molybdenum disulfide films with control over the layer number using a gas phase sulfur precursor. Nanoscale 2014;6(5):2821–6.

[68] Kibsgaard J, Chen Z, Reinecke BN, Jaramillo TF. Engineering the surface structure of MoS2 to preferentially expose active edge sites for electrocatalysis. Nat Mater 2012;11(11):963–9.

[69] Vikraman D, Park HJ. Shape-selective synthesis of NiO nanostructures for hydrazine oxidation as a nonenzymatic amperometric sensor. RSC Adv 2016;6(89):86101–7.

[70] Gong F, Wang H, Xu X, Zhou G, Wang Z-S. In situ growth of Co$_{0.85}$Se and Ni$_{0.85}$Se on conductive substrates as high-performance counter electrodes for dye-sensitized solar cells. J Am Chem Soc 2012;134(26):10953–8.

[71] Li S, Min H, Xu F, Tong L, Chen J, Zhu C, et al. All electrochemical fabrication of MoS$_2$/graphene counter electrodes for efficient dye-sensitized solar cells. RSC Adv 2016;6(41):34546–52.

[72] Kung C-W, Chen H-W, Lin C-Y, Huang K-C, Vittal R, Ho K-C. CoS acicular nanorod arrays for the counter electrode of an efficient dye-sensitized solar cell. ACS nano 2012;6(8):7016–25.

[73] Jung H, Koo B, Kim J-Y, Kim T, Son HJ, Kim B, et al. Enhanced photovoltaic properties and long-term stability in plasmonic dye-sensitized solar cells via non-corrosive redox mediator. ACS Appl Mater Interfaces 2014;6(21):19191–200.

[74] Hussain S, Patil SA, Vikraman D, Arbab AA, Jeong SH, Kim H-S, et al. Growth of a WSe$_2$/W counter electrode by sputtering and selenization annealing for high-efficiency dye-sensitized solar cells. Appl Surf Sci 2017;406:84–90.

[75] Huang S, Zai J, Ma D, Hu Z, He Q, Wu M, et al. Improving the catalytic performance of Ni$_3$S$_4$-PtCo heteronanorods via Mott-Schottky effect toward the reduction of iodine couples in dye-sensitized solar cells. Electrochim Acta 2017;241:89–97.